*Research Article*

# Verification of Imaging Algorithm for Signal Processing Software within Synthetic Aperture Radar (SAR) System

**Le-tian Zeng** [ID] **,[1,2] Chun-hui Yang,[1] Mao-sheng Huang,[1] and Yue-long Zhao[2]**

[1]*The Fifth Electronic Research Institute of MIIT, No. 110 Dongguanzhuang Road, Tianhe District, Guangzhou, China*
[2]*School of Computer Science and Engineering, South China University of Technology, Guangzhou University, Panyu District, Guangzhou, China*

Correspondence should be addressed to Le-tian Zeng; zengletian@ceprei.com

In the signal processing software testing for synthetic aperture radar (SAR), the verification for algorithms is professional and has a very high proportion. However, existing methods can only perform a degree of validation for algorithms, exerting an adverse effect on the effectiveness of the software testing. This paper proposes a procedure-based approach for algorithm validation. Firstly, it describes the processing procedures of polar format algorithm (PFA) under the motion-error circumstance, based on which it analyzes the possible questions that may exist in the actual situation. By data simulation, the SAR echoes are generated flexibly and efficiently. Then, algorithm simulation is utilized to focus on the demonstrations for the approximations adopted in the algorithm. Combined with real data processing, the bugs concealed are excavated further, implementing a comprehensive validation for PFA. Simulated experiments and real data processing validate the correctness and effectiveness of the proposed algorithm.

## 1. Introduction

Synthetic aperture radar (SAR) [1, 2] systems achieve high spatial resolutions by transmitting wide bandwidth linear frequency modulation (LFM) signal combined with long azimuth illumination time, which have been widely applied in both military and civilian areas. As digital technologies are continuously developing into maturity, the proportion of software within SAR systems is growing, so is that of functions implemented by software. Particularly, a large number of algorithms are necessary for SAR signal processing, such as beam forming and impulse compression. These signal processing algorithms account for a large proportion and are professional, which makes it difficult to find out the problems hidden. As a foundation for radar detection, the function and performance of SAR would be severely affected once the signal processing algorithms failed. To guarantee the quality [3–5] of SAR systems, it is indispensable to assure the quality of software in them. Hence, the validation for imaging algorithms is an important way to assure the software quality, which becomes a critical segment for SAR software testing [6–9].

In essence, the algorithm validation for SAR signal processing software mainly focuses on the adopted hypotheses together with approximations, the questions that may encounter in algorithm implementation, the processing performances under the circumstances of different parameters, and various external conditions. During the imaging algorithms, approximations can simplify the signal processing; however, they can simultaneously exert negative influences on the effective imaging scope and the final imaging results. In most cases, these influences are difficult to be accurately expressed by mathematical formula; instead, they need many trials to dig out the bugs deep inside the imaging algorithms. Moreover, SAR echoes are corrupted by noises, clusters, and interferences under a certain condition like the complicated combat environment, which imposes higher requirements for the adaptability and robustness for related processing algorithms.

Now, the algorithm validation for SAR signal processing software primarily utilizes the black box testing method: checking the collected SAR echoes with the help of simulators or real equipment and observing the imaging results

displayed on the interface so as to perform an indirect verification for the correctness of the algorithm implementation. However, this method can achieve a partial validation for the algorithms to some extent, dramatically decreasing the effectiveness of signal processing software testing.

In this paper, the validation of the imaging algorithm is organized as follows. The SAR echo data model and the procedure of polar format algorithm (PFA) are presented, figuring out the hypotheses and approximations that should be paid attention to in software testing. The improved concentric circle method (ICCM) is adopted to flexibly configure the system parameters and to quickly generate the SAR echoes needed. Then, the simulation experiments are designed to verify the correctness of PFA as well as its implementation in both motion-error-free and motion-error conditions, severally. Besides, considering the influences of external environment, real data processing is performed as a validation for real scenario to further inspect the performance, which can effectively complement the shortcomings of the former operations from a different perspective. Finally, simulation experiments and real data processing are employed to demonstrate the correctness and effectiveness of the proposed method.

## 2. SAR Echo Data Model and Processing Procedure for PFA

There are two kinds of SAR imaging algorithms: frequency-domain imaging algorithm and time-domain imaging algorithm. Frequency-domain imaging algorithm assumes that the SAR platform travels a perfect linear uniform acquisition trajectory. Approximations are usually made for dramatically decreasing the computational burden with slight precision degradation. Different frequency-domain imaging algorithms almost have an identical processing idea but vary at the way of approximations for range-azimuth decoupling. Widely applied in high-resolution spotlight SAR, the polar format algorithm (PFA) is a typical frequency-domain imaging algorithm and has the ability to accurately combine with autofocusing algorithms [10–12] to efficiently remove the residual phase errors. Associated theoretical derivations for PFA with line-of-sight polar interpolation (LOSPI) under motion-error condition are detailed in Reference [1].

Figure 1 describes the geometry of SAR echo data collection, where the antenna phase center (APC) moves along the $X$-axis (azimuth direction) with a constant velocity $v$ at $H$, forming an ideal trajectory as the dotted line illustrated. The radar beam operates in the squint angle $\theta_s$, and the instant corresponding to $N$, the center of the synthetic aperture, is at slow time $t_m = 0$. Construct a two-dimensional coordinate $XNR$ with the origin $N$. The coordinates of the scene center point target $O$ and an arbitrary target $P$ are $(R_s \sin \theta_s, R_s \cos \theta_s)$ and $(R_s \sin \theta_s + x, R_s \cos \theta_s + y)$, respectively, where $R_s$ is the reference range. Due to the presence of atmospheric turbulences and carrier perturbations, SAR platform travels a curve trajectory and
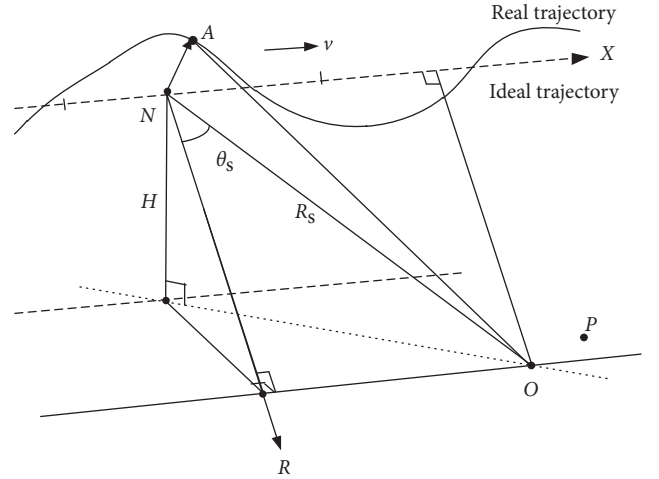


Figure 1: Geometry of SAR data collection.

the instantaneous slant range from the APC to $P$ can be expressed as

$$R(X; x, y) = R_0(X; x, y) + \Delta R(X; x, y), \qquad (1)$$

where $R_0(X; x, y) = \sqrt{(X - R_s \sin \theta_s - x)^2 + (R_s \cos \theta_s + y)^2}$ is the nominal instantaneous range between the APC and $P$, $X = v t_m$ signifies the instantaneous azimuth position of APC, and $\Delta R(X; x, y)$ represents the slant error.

Suppose radar transmits LFM signal, the received baseband radar echo can be given by

$$s(\tau, X; x, y) = \text{rect}\left[\frac{\tau - 2\Delta\tau}{T_p}\right] a_a(X) \times \exp\left[j\pi\gamma(\tau - 2\Delta\tau)^2\right]$$

$$\cdot \exp\left[-j2\pi f_c \Delta\tau\right], \qquad (2)$$

where $\text{rect}[\tau] = \begin{cases} 1, & |\tau| \leq 1/2, \\ 0, & |\tau| > 1/2, \end{cases}$ denotes the rectangular window function, $a_a(X)$ is the azimuth window function, $T_p$ is the impulse width, $\tau$ depicts the fast time, $\gamma$ means the chirp rate, $f_c$ defines the center frequency of the carrier, $\Delta\tau = 2R(X; x, y)/c$ indicates the double time delay from the APC to $P$, and $c = 3 \times 10^8$ m/s is the transmitted speed of the light in vacuum.

The flowchart of PFA processing is illustrated in Figure 2. In ideal case, range compression is firstly performed for the SAR echo data followed by azimuth dechirp. After the range interpolation and the azimuth interpolation, range inverse fast Fourier transform (IFFT) and azimuth IFFT are applied to generate a SAR image. It should be noted that the sampling rate in the range dimension changes after the range interpolation. Accordingly, the interval between the adjacent pixels in the range dimension changes and so does the range scope of the image. In the same way, the azimuth width of the image alters. Therefore, the scope of the final image should be paid attention to. In addition, the final imaged positions of the point targets have some certain deviations due to the limited validity of the underlying far-field approximation. The distortion manifests in geometric shifts as
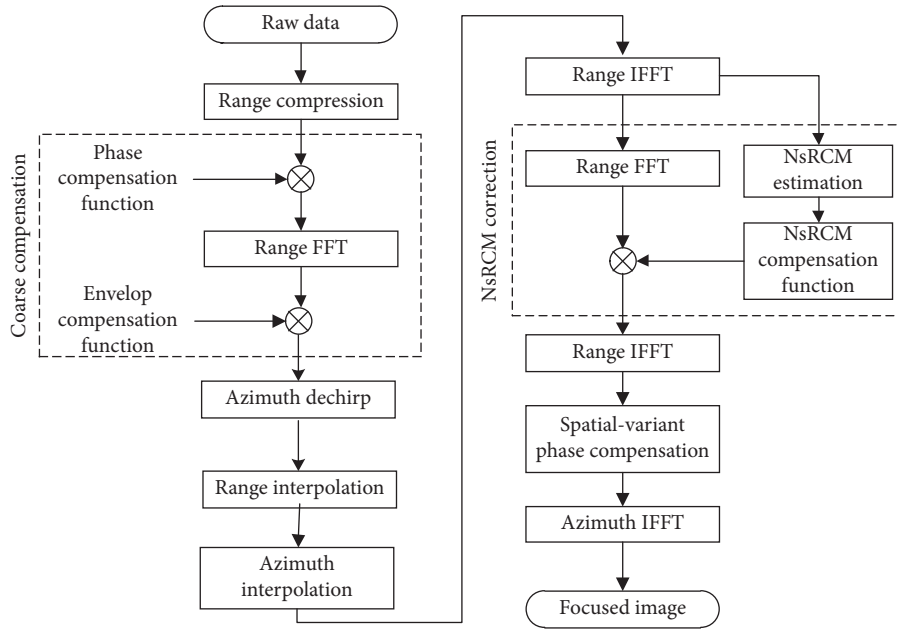
Figure 2: Flowchart for PFA processing.

well as in target defocusing and intensifies as distances between pixels and the scene reference position increase.

Actually, in order to eliminate these errors to an acceptable level, motion compensation (MOCO) must be included. By recording the relevant motion parameters with an onboard GPS or inertial measurement unit (IMU) system, the real movement of the SAR platform can be taken into account to carry out coarse compensation, i.e., removing most of the envelop errors and the phase errors of raw data. Nevertheless, the range interpolation and the azimuth interpolation change the forms of the remaining motion errors, resulting in an extra envelop deviation, i.e., nonsystematic range cell migration (NsRCM) [12], which may produce artifacts in the focused images if not properly accounted for in high-resolution imaging situation. All these factors should be considered when validating PFA.

In addition, PFA focuses at frequency domain in the azimuth with length being greater than that of the aperture during the data collection, which indicates PFA can be used in subaperture signal processing.

## 3. Procedure-Based Approach for the Validation of Imaging Algorithm

The procedure-based approach, which is based on a detailed analysis on flowchart for PFA, implements a comprehensive verification for SAR signal processing software from three aspects: echo data simulation, validation via algorithm simulation and verification by real data processing.

*3.1. Echo Data Simulation.* To achieve a rigorous validation for SAR imaging algorithms, echo data simulation is usually needed to efficiently generate the SAR echoes. In this paper,

the improved concentric circle method (ICCM), which can flexibly configure the system parameters, is utilized to simulate point target echoes and distributed scene target echoes with a high accuracy and efficiency. Details for the ICCM are presented in Reference [13].

*3.2. Validation via Algorithm Simulation.* Validation via algorithm simulation encompasses point target simulation and distributed scene target simulation. Combined with the flowchart of PFA, validation via algorithm simulation not only focuses on the effective scope of the imagery as well as the final focusing results of the point targets under ideal circumstances but also emphasizes on the approximations along with accuracies of motion compensation due to unpredicted platform motion or other propagation delays. Thereinto, point target simulation can detect the problems hidden in the algorithm implementation promptly and reflect the probable defects of the algorithm accurately, which play a significant role in verifying SAR imaging algorithms.

*3.2.1. Validation via Algorithm Simulation under Motion-Error-Free Condition.* Due to the planar wave-front approximation [1], the focusing positions of point targets present certain fluctuations to some extent after strictly circling $\theta_s$ counterclockwise, inducing distortions of the image. With the increasing range to the scene center, the focusing results of the associated targets become worse.

With LOSPI, the azimuth impulse response function (IRF) of the point target is distributed in only a single range bin and also normal to the range IRF. The focusing result of the point target can be evaluated via the peak side-lobe ratio (PSLR), the integrated side-lobe ratio (ISLR), and the impulse response width (IRW). PSLR refers to the proportion

of the energy of first side lobe to that of the main lobe, which is denoted in decibel (dB) by

$$\text{PSLR} = 10 \lg \frac{\int_{\text{first side lobe}} |h(x,y)|^2 dx}{\int_{\text{main lobe}} |h(x,y)|^2 dx}. \tag{3}$$

ISLR is the proportion of the energy of all side lobes to that of the main lobe, which yields

$$\text{ISLR} = 10 \lg \frac{\int_{\text{side lobes}} |h(x,y)|^2 dx}{\int_{\text{main lobe}} |h(x,y)|^2 dx}, \tag{4}$$

where $h(x,y)$ depicts the IRF of a certain point target. Besides, the intervals between two adjacent pixels change after the interpolation operations. Correspondingly, the scope of the imaging area should be recalculated.

For the distributed scene targets, the whole performance for the imagery can be measured by entropy and contrast. While entropy of the image indicates its gray-level distribution, contrast of the image tends to concentrate energy that has been blurred out by a phase distortion, which can be defined by

$$\text{entropy} = \frac{1}{\text{nrn} \times \text{nan}} \sum_{n=1}^{\text{nan}} \sum_{i=1}^{\text{nrn}} \log_2 |s(i,n)|,$$

$$\text{contrast} = \frac{1}{\text{nrn}} \sum_{i=1}^{\text{nrn}} \frac{\sigma_i}{\mu_i}, \tag{5}$$

where $s(i,n)$ is the signal value of the $i$th $(i = 1, 2, \ldots, \text{nrn})$ row and the $n$th $(n = 1, 2, \ldots, \text{nan})$ column of a focused image, nrn and nan are the number of the range bins and that of the azimuth bins. $\mu_i = (1/\text{nan}) \sum_{n=1}^{\text{nan}} |s(i,n)|$ and $\sigma_i = \sqrt{(1/\text{nan}) \sum_{n=1}^{\text{nan}} (|x(i,n)| - \mu_i)^2}$ represent the mean value and the standard deviation of the amplitudes for the pixels within the $i$th range bin, respectively. Generally, the smaller the entropy, the better the imaging results; the greater the contrast, the better the focusing effects.

### 3.2.2. Validation via Algorithm Simulation under Motion-Error Condition.

Validation via algorithm simulation under motion-error condition mainly includes the verifications for motion errors after two-dimension interpolation, the accuracies for NsRCM correction, and phase compensation.

The two-dimensional interpolation operation changes the forms of motion errors, resulting in an alteration to the envelop of the phase-history-domain signal. That is, significant defocusing exists if the NsRCM were not properly cancelled. To lower overall computational burden, approximations are always made for NsRCM and their accuracies can be assessed from two aspects: (1) observing whether the envelop of the phase-history-domain signal after NsRCM correction is restricted in a single range bin; (2) evaluating the final focusing performance via some representative indicators, such as PSLR, ISLR, and IRW.

Actually, phase errors have diverse forms for the targets that are located in different positions, i.e., the spatial variance of the phase errors. When a uniform compensation is carried out, the residual phase errors may have an undesirable effect on the focusing performance and should be taken into account. We can roughly estimate the value range of the residual phase errors after the coarse compensation according to the accuracy of the GPS or inertial navigation system (INS). Then, we choose targets that are far away from the scene center, compensate for their phase errors with uniform and spatially variant corrections, respectively. Herein, spatially variant compensation can be implemented by dividing the phase-history-domain data into even blocks in the range dimension and correcting the corresponding phase errors one by one. Finally, we can draw a conclusion from the whole focusing performance of the final image as well as local focusing results of strong scatters.

### 3.3. Verification by Real Data Processing.

In real SAR echo data, the true motion errors are unknown and the instantaneous positions of the SAR platform can only be obtained with the help of the measuring equipment. Compared with simulation data, real data are collected in real scenario and usually corrupted by unknown clutters, uncertain noises, and different interferences. Hence, real data processing can be regarded as the validation of imaging algorithm in actual situation, which plays an important role that point target simulation and the distributed scene target simulation cannot replace. The results of real data processing not only are good indicators for the performance and robustness of the imaging algorithm but also become a critical complement to algorithm simulation. Only when bugs do not exist in the algorithm simulation can real processing be conducted.

When dealing with the real data processing, motion errors should be preliminarily removed according to the GPS/INS information. Combined with corresponding autofocusing algorithms [10, 11], such as weighted phase gradient autofocus (WPGA), the motion errors can be corrected further. In general, the effects for real data processing are directly related to the accuracy of the motion compensation. The more accurate the motion compensation is, the better the focusing performance becomes.

While entropy and contrast can be utilized to judge the whole performance for the final results of the real data processing, specific corner reflectors are chosen to validate the focusing effects of strong scatters within the image. The two corner reflectors next to each other and distributed in a single range bin are usually extracted and interpolated to clearly reflect whether their main lobes of IRFs can be separated and to determine the azimuth resolution of the final image. Furthermore, PSLR, ISLR, and IRW can be determined by extracting the corner reflector that is distributed in a single range bin and implementing an interpolation operation. Due to the existences of the clusters, noises, and interferences, sharpening window functions [1] are usually adopted in range compression and azimuth compression to constrain the side lobes. Generally, the PLSR and ISLR are under $-20\,\text{dB}$ and $-17\,\text{dB}$, respectively.
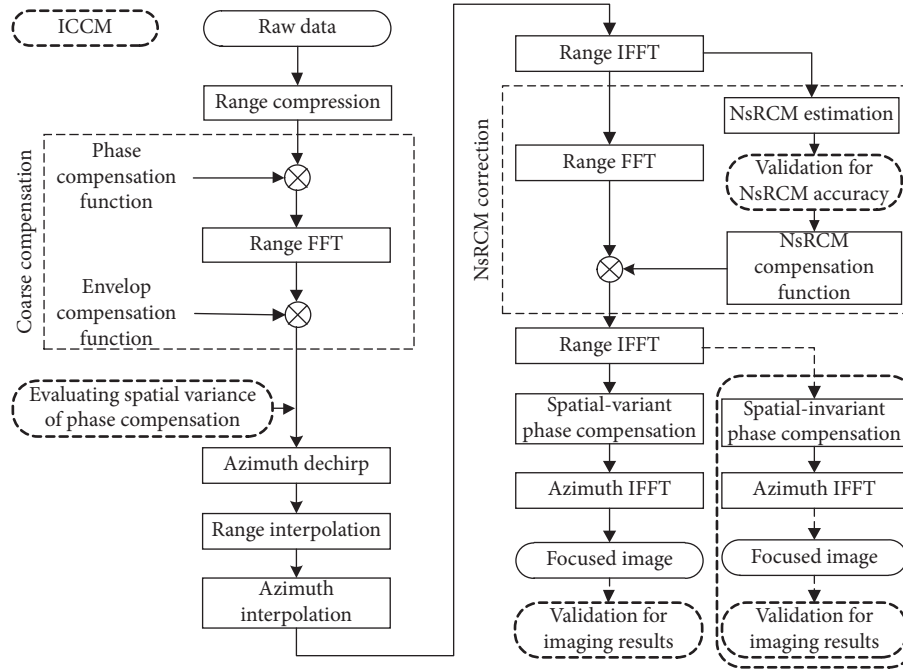
Figure 3: Procedure-based validation for PFA within SAR signal processing software testing.

To sum up, the procedure-based validation for PFA within SAR signal processing software testing is depicted in Figure 3.

## 4. Experimental Results

In this part, echo data simulation, algorithm simulation experiments, and real data processing experiments are developed, focusing on the bugs that are easy to exist in SAR signal processing software, digging out the bugs concealed in the imaging algorithm from different perspectives and validating the effectiveness of the proposed method.

*4.1. Echo Data Simulation.* The SAR platform travels with a constant velocity $v$ along the right direction of $X$-axis at the height of $H$, forming a synthetic aperture BC, as presented in Figure 4. $N$ is the center of BC, $W_r$ and $W_a$ are the widths of the illuminated area in the azimuth and its perpendicular direction on the ground, respectively. Simulation parameters are shown in Table 1.

To demonstrate the high efficiency of generating SAR echoes, point-by-point scanning (PBPS) and ICCM are separately adopted to simulate echo data for $10 \times 10$, $20 \times 20$, $40 \times 40$, $80 \times 80$, $100 \times 100$, and $200 \times 200$ point targets. The sampling number in the range direction is 8192 and that in the azimuth direction is 4096. The elapsed time by the two methods is depicted in Figure 5, where the horizontal axis represents base-10 logarithmic for the number of the point targets and the vertical coordinate signifies the corresponding time consumed. Obviously, with the dramatic increasing of the number of point targets, PBPS consumes much more time than ICCM, whose time curve has a relatively gentle growth and means a much higher efficiency than PBPS.
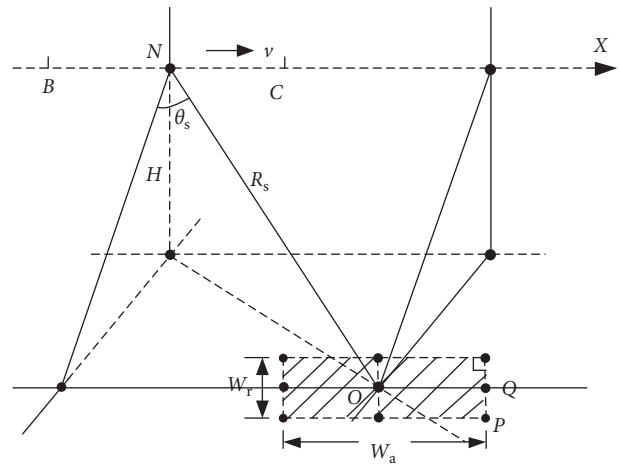


Figure 4: Geometry of echo data collection.

*4.2. Validation by Simulation Experiments.* Algorithm simulation experiments include verification via PFA simulation under ideal circumstance, validation for the effects of motion error, and verification of distributed scene targets.

*4.2.1. Verification via PFA Simulation under Ideal Circumstance.* In this simulation experiment, spotlight SAR works in the squinted mode and system parameters are presented in Table 2. The length of the synthetic aperture is 512 m and the number of echoes is 4096, achieving a high-resolution SAR image on the slant plane $NP_0O$. The theoretical values of the range resolution and the azimuth resolution are 0.25 m and 0.21 m, respectively. $W_a = 350$ m and $W_r = 450$ m depict the scope of point targets on the ground, each of which has an interval of 50 m in both directions as

TABLE 1: Simulation parameters.

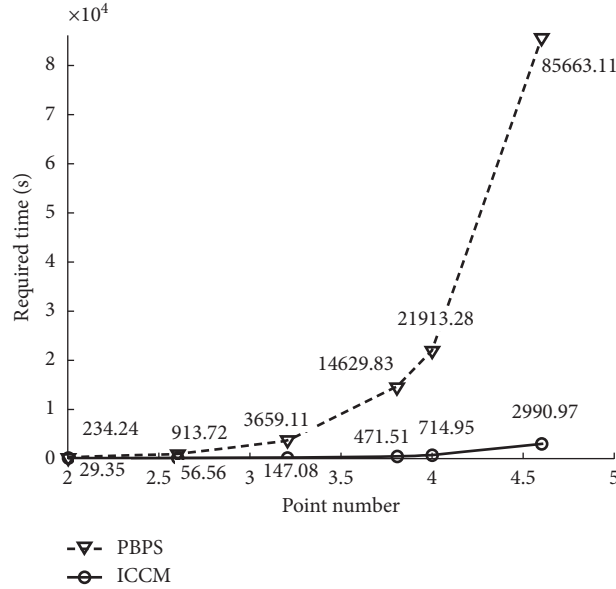| Parameter | Carrier frequency (GHz) | Pulse width (μs) | Bandwidth (MHz) | Sampling rate (MHz) | Velocity (m/s) | Slant range (km) | Squint angle (deg) | PRF (Hz) | Height (km) |
|---|---|---|---|---|---|---|---|---|---|
| Value | 9.6 | 1 | 600 | 800 | 100 | 12 | 30 | 800 | 5.7 |



FIGURE 5: Time consumed by echo data simulation.

TABLE 2: Simulation parameters.

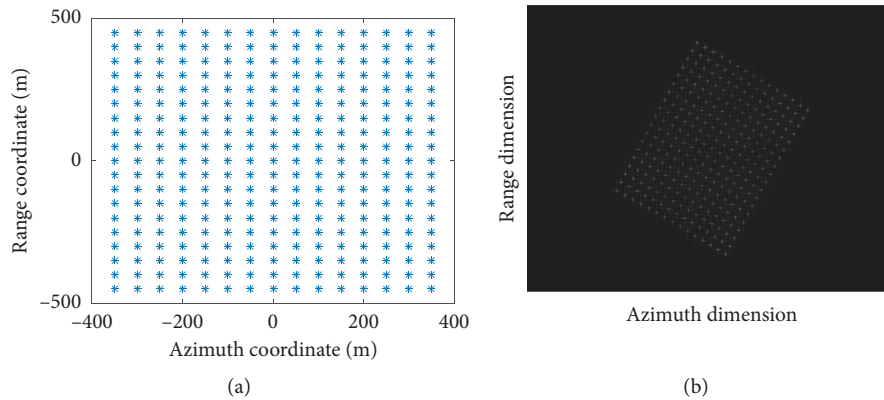| Parameter | Carrier frequency (GHz) | Pulse width (μs) | Bandwidth (MHz) | Sampling rate (MHz) | Velocity (m/s) | Slant range (km) | Squint angle (deg) | PRF (Hz) |
|---|---|---|---|---|---|---|---|---|
| Value | 9.6 | 1 | 600 | 720 | 100 | 6 | 30 | 800 |



FIGURE 6: Sketch map of the point target distribution and related imaging result.

Figure 6(a) shows. Figure 6(b) gives the imaging result after PFA processing. Accordingly, the analyzes on the results of the scene center point target $O$ together with other point targets, like $P$ and $Q$, are illustrated in Figures 7(a)–7(f).

In Figure 6, the horizontal and vertical coordinates have some certain deviations from their theoretical positions except for the scene center point target $O$. Moreover, the focusing positions of $P$ and $Q$ are presented in Table 3, from which we can see that the deviation increases with the range to $O$. From the contour maps in Figure 7, $O$ focuses well but the main lobes in the azimuth for $P$ and $Q$ intertwine their first side lobes. The PSLR, ISLR, and IRW are listed in Table 4, which signifies that the focusing performance degrades as the range to the scene center increases.
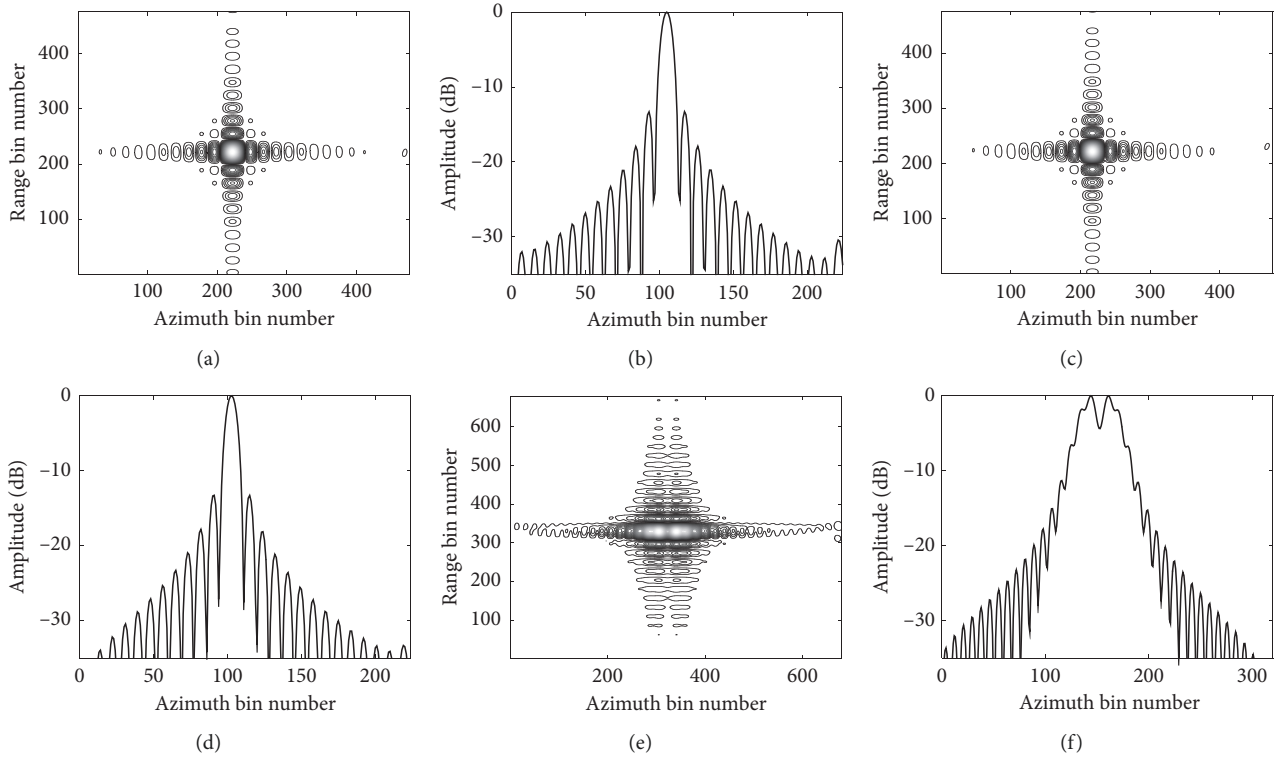
Figure 7: Analyses on results of $O$, $P$, and $Q$: (a) contour map of $O$; (b) azimuth IRF of $O$; (c) contour map of $Q$; (d) azimuth IRF of $Q$; (e) contour map of $P$; (f) azimuth IRF of $P$.

Table 3: Focusing positions of $P$ and $Q$.

| Point target | Point location (m) | Ideal positions after PFA processing (m) | Actual positions after PFA processing (m) | Position deviations (m) |
|---|---|---|---|---|
| Target $Q$ | (100, 50) | (61.60, 93.30) | (61.11, 93.45) | (−0.49, 0.15) |
| Target $P$ | (350, −450) | (528.11, 214.71) | (530.27, −202.95) | (2.16, 11.76) |

Table 4: Analyses on imaging results.

| | Range direction | | | Azimuth direction | | |
|---|---|---|---|---|---|---|
| | PSLR (dB) | ISLR (dB) | IRW (m) | PSLR (dB) | ISLR (dB) | IRW (m) |
| Target $O$ | −13.25 | −10.11 | 0.21 | −13.29 | −10.22 | 0.17 |
| Target $Q$ | −13.27 | −10.14 | 0.21 | −13.28 | −10.24 | 0.22 |
| Target $P$ | −13.16 | −9.91 | 0.21 | −0.01 | 3.36 | 0.53 |

### 4.2.2. Validation for the Effects of Slant Range Error

*Experiment 1.* In this part, SAR echo data simulation is performed according to the parameters in Table 1. During the data collection, a uniform slant error function is added to the ideal range of each point target, as indicated in Figure 8(a). PFA is utilized to process the echo data according to Figure 2. Without NsRCM correction but with phase error cancellation, the azimuth IRF profile of $O$ is shown in Figure 8(b). To demonstrate the correctness for compensating for NsRCM, the first-order approximation to NsRCM is made and adopted to correct the envelop error of the phase-history-domain signal, accomplishing the azimuth IRF profiles of $O$ and $P$ as illustrated severally in Figures 8(c) and 8(d).

It can be observed that without NsRCM correction, the azimuth IRF of $O$ still has significant defocusing although phase error compensation is performed. With NsRCM correction and phase error cancellation, the focusing performance for the azimuth IRFs of $O$ and $P$ has greatly improved, with PSLR −13.07 dB and −12.84 dB and ISLR −10.25 dB and −10.07 dB, respectively. Clearly, PSLR and ISLR are close to their standard values, which confirms the reasonability for the first-order approximation to NsRCM.

*Experiment 2.* In practice, SAR platform cannot strictly move along a straight line at a constant velocity. Motion errors exert different influences on the point targets located in various positions. The residual errors have different values if uniform phase error compensation is performed. To
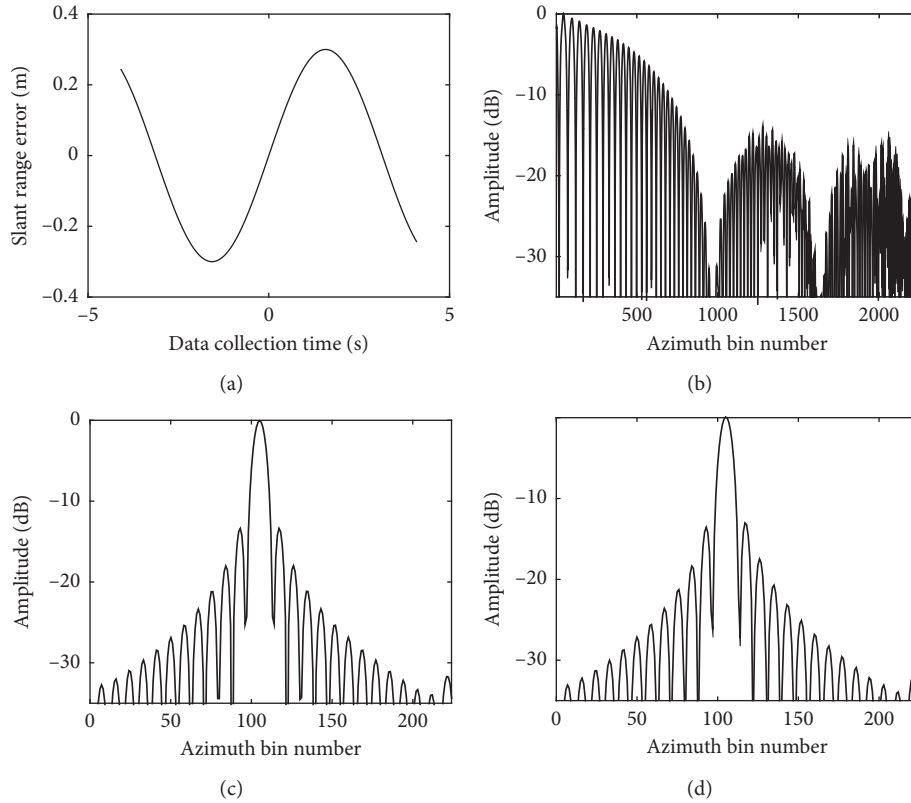
(a)

(b)

(c)

(d)

FIGURE 8: Imaging results with uniform slant range error: (a) added slant range error; (b) azimuth IRF profile of $O$ without NsRCM correction; (c) azimuth IRF profile of $O$ with NsRCM correction; (d) azimuth IRF profile of $P$ with NsRCM correction.

estimate the effects of the spatial variances of the phase errors, we add a three-dimensional motion error to the ideal trajectory of the SAR platform shown in Figure 9(a). Other conditions are the same to those in Experiment 1. PFA is employed to process the SAR echo data, within which uniform and spatial-variant phase error corrections are performed for the phase-history-domain data, separately. The contour maps of $P$ with uniform phase error correction and with spatially variant phase error cancellation are given in Figures 9(b) and 9(c), respectively. Correspondingly, we obtain the azimuth IRF profiles of $P$ under no MOCO, uniform correction, and spatial-variant cancellation circumstances, which is illustrated in Figure 9(d).

By calculation, the entropies of Figures 9(b) and 9(c) are 2.45 and 2.13, separately. Smaller entropy means better focusing result, which demonstrates the necessity of removing the spatial variances of phase errors in high-resolution spotlight SAR imaging. In Figures 9(d), the azimuth IRF profile of $P$ is much better in focusing performance after the spatial-variant phase error compensation. The PSLR and ISLR of $P$ are −6.80 dB and −6.82 dB after uniform phase error correction, respectively. For comparison, the PSLR and ISLR of $P$ are −13.35 dB and −10.44 dB after spatial-variant phase error correction, separately, much closer to each standard value. In summary, this experiment indicates spatial-variant phase error correction can produce a higher quality image.

*4.2.3. Verification by Distributed Scene Targets.* In this part, we use simulation parameters in Table 5 to generate SAR echoes of the distributed scene targets by ICCM. To verify the subaperture imaging performance of PFA, we employ PFA, modified Omega-K algorithm [14, 15], and frequency nonlinear chirp scaling (FNCS) [16] algorithm to process these echoes, achieving the imaging results shown in Figures 10(a)–10(c), respectively. The horizontal direction is the azimuth direction, and the vertical direction is the range direction.

During the SAR data collection, the length of the aperture in the azimuth is 502° m and the width in the azimuth of the scene is 491° m. After PFA processing, the associated width in the azimuth becomes 1009° m, which is much greater than that of the aperture in the azimuth. Moreover, the focusing domain of the final image is the frequency domain in the azimuth dimension, presenting the typical characteristic of subaperture signal processing and indicating that PFA is fit for subaperture imaging. With the modified Omega-K algorithm, the width in the azimuth of the final image is 337° m, less than that in the azimuth of the scene, inducing a serious folding of the imaging result. With FNCS algorithm, the entropy and the contrast are 12.39 and 2.19, respectively. They are very close to the values (with entropy 12.38 and contrast 2.28) obtained by PFA, which means sound performance for PFA to deal with subaperture echoes.
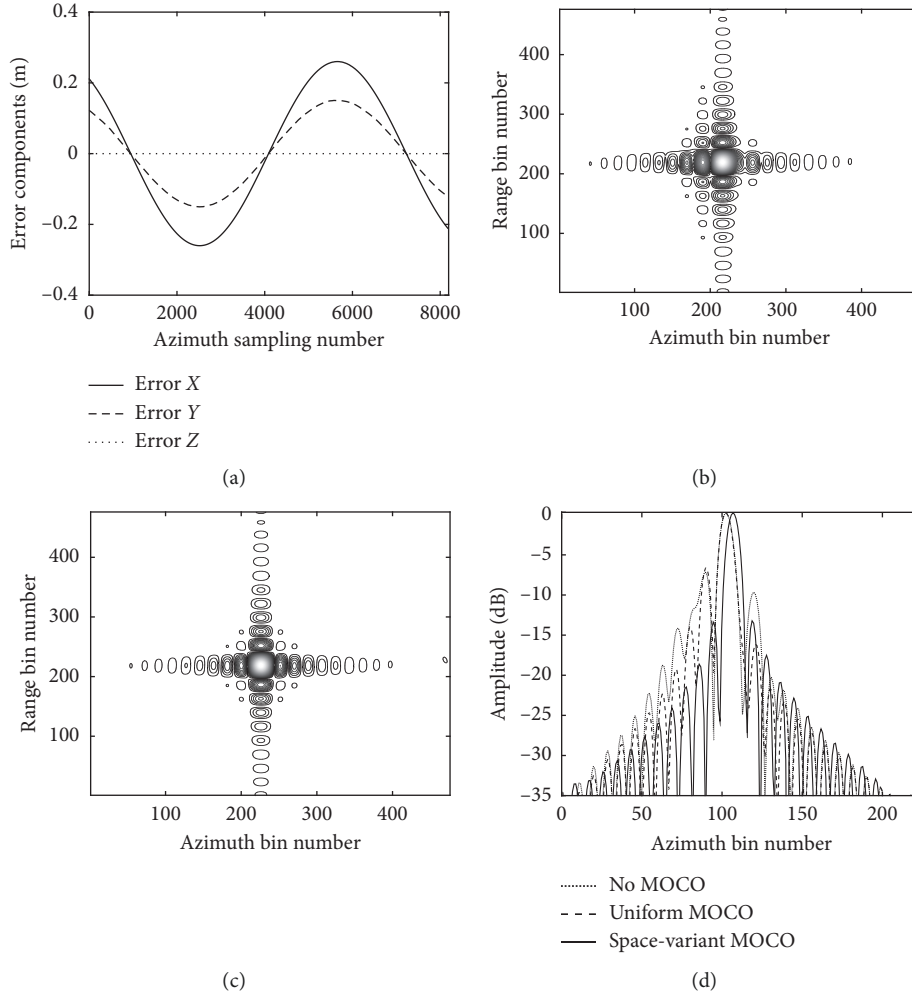
(a)



(b)



(c)



(d)

FIGURE 9: Motion errors and imaging results: (a) motion errors added in $X$, $Y$, and $Z$ dimensions; (b) contour map of $P$ with uniform phase error correction; (c) contour map of $P$ with spatially variant phase error correction; (d) azimuth IRF profile of $P$ under different conditions.

TABLE 5: Simulation parameters.

| Parameter | Carrier frequency (GHz) | Pulse width ($\mu$s) | Bandwidth (MHz) | Velocity (m/s) | Slant range (km) | Squint angle (°) | Range sampling number | Azimuth sampling number |
|---|---|---|---|---|---|---|---|---|
| Value | 9.6 | 1 | 300 | 100 | 12 | 30 | 1638 | 2510 |

*4.3. Demonstration through Real Data Processing.* In this section, we perform a real data experiment to investigate the feasibility of the PFA. The data set is acquired by X-band SAR working in the spotlight mode. The data set contains 4096 echoes, each of which has 4096 sampling numbers in the range dimension. The theoretical values in both range and azimuth dimensions are about 1.2 m and 0.82 m with the broadening effects of window functions being taken into account. The SAR imaging result implemented by PFA has serious defocusing without MOCO as shown in Figure 11(a). The reconstructed image without NsRCM correction and with "NsRCM correction + spatially variant phase error compensation are illustrated in Figures 11(b) and 11(c), respectively. The entropies of Figures 11(a)–11(c) are 14.55, 12.22, and 12.08 in the listed order. Smaller entropy means better focusing performance.

To clearly reflect the improvement for the focusing performance with PFA flowchart in Figure 2, subscenes extracted from the same area (the dotted rectangle in Figure 11(c)) in Figures 11(a)–11(c) are amplified, corresponding to Figures 12(a)–12(c) with entropies 10.37, 3.73, and 3.36, separately. It is evident that PFA "NsRCM correction + spatially variant phase error compensation" reaches a satisfactory result. To further verify the performance of azimuth resolution, a strong scatter target is extracted from the same areas of Figures 12(a)–12(c), as shown in the dotted ellipse in Figure 12(c). The azimuth IRFs of the strong scatter target is plotted in Figure 12(d). Apparently, a promising result, in forms of good side-lobe supression and azimuth resolution, is achieved with NsRCM correction and spatially variant phase error compensation. Thus, this experiment
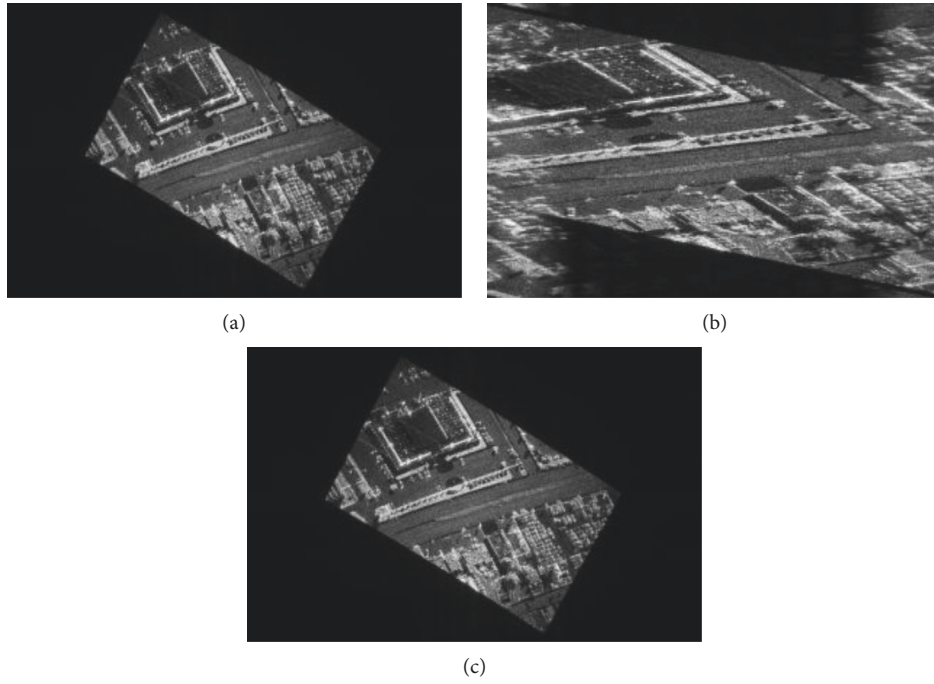
(a)



(b)



(c)

FIGURE 10: Imaging results of distributed scene targets (a) with PFA, (b) with modified Omega-K algorithm, and (c) with FNCS algorithm.
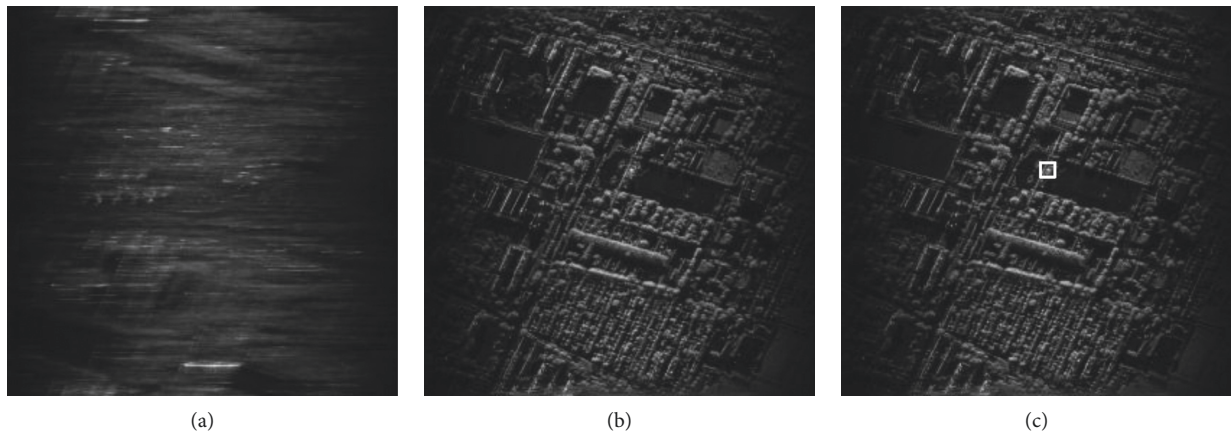


(a)



(b)



(c)

FIGURE 11: Real data processing results (a) without MOCO, (b) without NsRCM correction, and (c) with NsRCM correction and spatially variant phase error compensation.
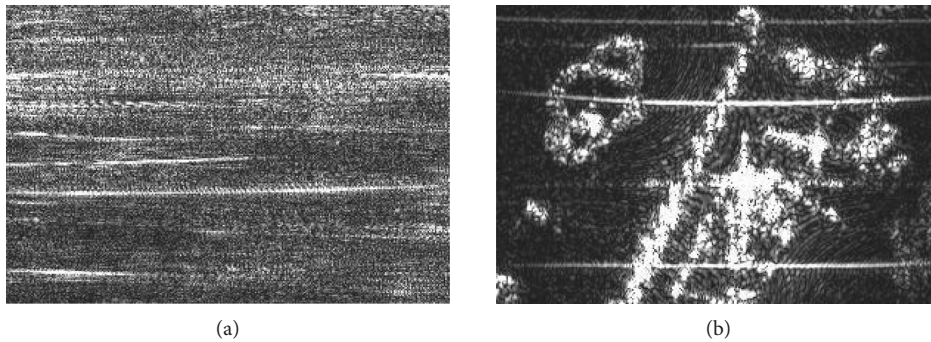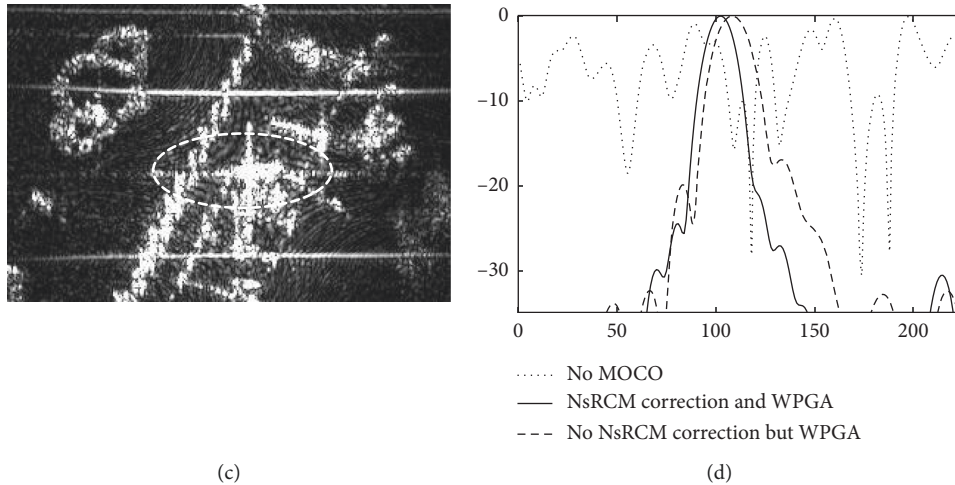


(a)



(b)

FIGURE 12: Continued.

(c)



...... No MOCO

―――― NsRCM correction and WPGA

- - - No NsRCM correction but WPGA

(d)

FIGURE 12: Subscene imaging results and azimuth IRF: (a) subscene from Figure 11(a); (b) subscene from Figure 11(b); (c) subscene from Figure 11(c); (d) azimuth IRF of strong scatter point in dotted ellipse of (c).

confirms the necessity and correctness of the PFA from the real scenario perspective.

## 5. Conclusions

In this paper, a procedure-based validation approach is proposed for SAR signal processing algorithms. The echo data model and processing flowchart for PFA are analyzed, pointing out the corresponding hypotheses and approximations. Combined with algorithm simulation and real data processing, different questions that may exist in the algorithm implementation are validated specifically and pointedly, comprehensively verifying the correctness and effectiveness of signal processing algorithms within SAR software. It should be noted that the proposed approach also works well on higher carrier frequency (such as Ku/Ka band) instead of ultra-wideband SAR imaging situation, where the planar wave-front hypothesis does not hold and the non-orthogonal side lobes appears. The verifications of signal processing algorithms for SAR-ground moving target identification (GMTI) will be subject of future work.

## Data Availability

The raw/processed data required to reproduce these findings cannot be shared at this time as the data also form part of an ongoing study and are used under license for the current study.

## Conflicts of Interest

The authors declare that there are no conflicts of interests regarding the publication of this paper.
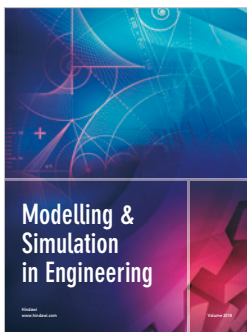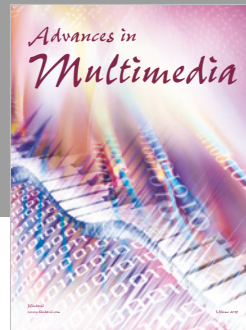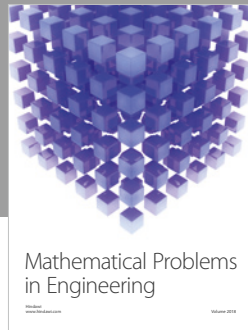
## Acknowledgments

## References

[1] W. G. Carrara, R. S. Goodman, and R. M. Majewski, *Spotlight Synthetic Aperture Radar Signal Processing Algorithms*, Artech House, Bloomington, IN, USA, 1995.

[2] B. Zheng, M. D. Xing, and T. Wang, *Radar Imaging Technology*, Publishing House of Electronics Industry, Beijing, China, 2005.

[3] I. Mistrik, R. Soley, N. Ali et al., *Software Quality Assurance in Large Scale and Complex Software-Intensive Systems. Chapter 1*, Morgan Kaufmann, Burlington, MA, USA, 2016.

[4] J. D. Musa, *Software Reliability Engineering: More Reliable Software Faster and Cheaper*, Author House, Bloomington, IN, USA, 2004.

[5] X. H. Yang, *How to enhance the Value of Software Testing*, China Machine Press, Beijing, China, 2017.

[6] J. Itkonen, M. Mantyla, M. V. Mantyla, and C. Lassenius, "The role of the tester's knowledge in exploratory software testing," *IEEE Transactions on Software Engineering*, vol. 39, no. 5, pp. 707–724, 2013.

[7] M. Harman, S. A. Mansouri, and Y. Zhang, "Search-based software engineering," *ACM Computing Surveys*, vol. 45, no. 1, pp. 1–61, 2012.

[8] A. Bertolino, "Software testing research: achievements, challenges, dreams," in *Proceedings of 2007 IEEE Future of Software Engineering (FOSE'07)*, pp. 85–103, Minneapolis, MN, USA, May 2007.

[9] S. M. Zhu, *Software Testing Method and Technology*, Tsinghua University Press, Beijing, China, 2014.

[10] J. Kolman, "PACE: an autofocus algorithm for SAR," in *Proceedings of IEEE International Radar Conference*, Arlington, VA, USA, May 2005.

[11] W. Ye, T. S. Yeo, and Z. Bao, "Weighted least-squares estimation of phase errors for SAR/ISAR autofocus," *IEEE Transactions on Geoscience and Remote Sensing*, vol. 37, no. 5, pp. 2487–2494, 1999.

[12] X. Mao, D. Zhu, and Z. Zhu, "Autofocus correction of APE and residual RCM in spotlight SAR polar format imagery," *IEEE Transactions on Aerospace and Electronic Systems*, vol. 49, no. 4, pp. 2693–2706, 2013.

[13] L. T. Zeng, C. H. Yang, Y. L. Zhao, P. Chen, and Q. Wang, "A novel testing method for narrowband synthetic aperture radar (SAR) imaging algorithm," in *Proceedings of International Conference on Dependable Systems and Their Applications (DSA)*, pp. 66–72, Beijing, China, October 2017.

[14] J. Hippler, "High resolution processing with the rotated omega-k-algorithm applied to smartradar spot SAR data," in *Proceedings of 8th European Conference on Synthetic Aperture Radar*, pp. 1–3, Aachen, Germany, June 2010.

[15] N. Mishra and S. S. Medasani, "Extended omega-K algorithm for high squint mode airborne SAR imaging with motion compensation," in *Proceedings of 2014 IEEE International Microwave and RF Conference (IMaRC)*, pp. 352–355, Bangalore, India, December 2014.

[16] Y. Liang, Z. Li, L. Zeng, M. Xing, and Z. Bao, "A high-order phase correction approach for focusing HS-SAR small-aperture data of high-speed moving platforms," *IEEE Journal of Selected Topics in Applied Earth Observations and Remote Sensing*, vol. 8, no. 9, pp. 4551–4561, 2015.